Enhanced mid-infrared gas absorption spectroscopic detection using chalcogenide or porous germanium waveguides

Rami Zegadi, Nathalie Lorrain, Lo c Bodiou, Mohammed Guendouz, Lahcene Ziet, Joël Charrier

Enhanced Mid-Infrared gas absorption spectroscopic detection using Chalcogenide or porous germanium waveguides.

Rami Zegadi [1,2], Nathalie Lorrain [1], Loïc Bodiou [1], Mohammed Guendouz [1], Lahcene Ziet [2] and Joël Charrier [1]

[1] Univ Rennes 1, CNRS, Institut Foton – UMR 6082, F-22305 Lannion, France
[2] Department of Electronics, Faculty of Technology, LEPCI laboratory, Ferhat Abbas University Sétif 1, 19000, Sétif, Algeria

E-mail: ramizegadi@univ-setif.dz

Received xxxxxx
Accepted for publication xxxxxx
Published xxxxxx

Abstract

Different integrated photonic sensors are investigated for the detection in the mid-infrared region of the two gases namely carbon dioxide (CO_2) and methane (CH_4). The three studied structures are ridge waveguides, based both on chalcogenide films (ChG) or porous germanium (PGe) and slot waveguides based on ChG. Waveguide dimensions are optimized to obtain the highest power factor between guided light and gas while maintaining a single mode propagation in the mid-infrared wavelength range. The achievable power factor is 1% in case of ChG ridge-waveguide, 45% for PGe-ridge, and 58% in case of ChG-slot. Extremely low limits of detection (LOD), 0.1 ppm for carbon dioxide at λ= 4.3 μm and 1.66 ppm for methane at λ= 7.7 μm are obtained for a ChG slot waveguide, due to the large gas absorption coefficients in the mid-infrared spectral range. For porous germanium waveguides, low LOD values are also computed: 0.12 ppm for CO_2 at λ= 4.3 μm and 1.89 ppm for CH_4 at λ= 7.7 μm. These results show that the proposed structures could achieve competitive performance required for generic spectroscopic detection on a chip for environment and health sensing.

Keywords: Mid-Infrared detection; Integrated optical sensors; Power factor; Design; Ridge and slot waveguides; Chalcogenide and Porous germanium materials.

1. Introduction

In recent years, chemical sensing has emerged as an important application for integrated photonics outside of optical communication. The detection of noxious and flammable gases becomes necessary at from both domestic and industrial point of views. Gas sensors can be used to detect different types of gases and have therefore found applications in various fields in particular chemistry, health, biology, agriculture and environment [1]. The mechanism of detection can depend on thermal, chemical, mechanical, electrical or optical properties of functional materials [2]. Nevertheless, high-end spectroscopic systems often require laboratories that would use free space configurations to measure the absorption spectra of gas molecules inside a measurement chamber. These systems could be considered cumbersome and expensive, which is considered as the first disadvantage [3–10]. The second major disadvantage of these sensors comes from their size, which impedes on-field

deployment. Integrated optical sensors are a promising alternative to avoid these drawbacks [11]. With their immunity to electromagnetic interference, low power consumption, compactness, lightweight, and remote sensing ability, these sensors are adequate tools to detect different types of gases. In addition, the response time with high sensitivity, low Limit of Detection (LOD) and large reusability make them indispensable for the realization of lab-on-chip systems that are both cheap and portable.

The mid-infrared (Mid-IR), which is defined as the wavelength range of the electromagnetic spectrum between 2 and 20 µm, contains absorption peaks for a wide variety of gases including H_2O, CO, CO_2, NO, NO_2, CH_4 [3,12–14]. For example, carbon dioxide (CO_2) displays strong absorption features around 4.3 µm and methane (CH_4) exhibits two strong absorption at 7.7 and 3.3 µm [15]. The challenge is then to design highly sensitive sensors of lab-on-chip size that can be integrated into embedded circuitry for controlling systems.

Photonic integrated circuits operating in the Mid-IR range have already been implemented using the mature technology offered by III-V and group IV semiconductors. These devices have taken advantage of the Mid-IR transparency of silicon (2–8 µm) [16], germanium (2-14 µm) [17,18], and gallium arsenide (2-16 µm) [19] to integrate passive components at chip level [7,17,20–22]. Other materials such chalcogenide glasses (ChG) could also be used. They are amorphous semiconductors and contain elements such as tellurium, selenium or sulphur covalently bonded with As, Ge, Sb, and Ga [23]. They can be doped with rare earth ions [24] and processed as fibers, thin films or integrated waveguides displaying a broad transparency extending towards the mid-IR, up to 12 µm, 15 µm and 20 µm respectively for sulphide, selenide and telluride glasses [7]. Mid-IR supercontinuum generation and sensing have been demonstrated using ChG fibers [25,26]. Integrated Mid-IR chalcogenide devices have been fabricated on different substrates such as silicon (Si) [27], calcium fluoride (CaF_2) [28], sulphide glass (As_2S_3) [29], sodium chloride (NaCl) [30], lithium niobate ($LiNbO_3$) [31] for surface enhanced infrared absorption spectroscopy (SEIRAS) [32,33] or directly integrated with Quantum Cascade Laser (QCL) chips [34]. The feasibility of chemical-biological sensing in gas and liquid environment exploiting Mid-IR sensing based on undoped chalcogenides [5,35]and on the luminescence from rare-earth doped chalcogenide integrated platforms have been proposed and demonstrated [36,37].

Several platforms have been studied for optical detection. These include waveguides, Mach-Zehnder interferometers, micro-ring resonators and microcavities in the near-infrared range [38,39]. The detection principle is based on the change in refractive index. In case of gas detection, the refractive index variation is very small and, therefore, these refractive index changes are not the most reliable parameters to exploit. On the contrary, the detection of gases by absorption and consequent reduction of the transmitted intensity in the guiding structures is particularly interesting in the Mid-IR range. The key point of volume absorption in gas sensors is based on the increased interaction of light and gas infiltrated into the pores, which has to be maximized. The use of ridge and slot waveguides should maximize the power factor ratio value. Moreover, the use of integrated waveguide made of porous materials could also enhance the light-gas interaction [40].

In this work, an analytical design of an evanescent optical field sensor working in the Mid-IR spectral domain is provided for detection of CO_2, and CH_4. The objective is to optimize the detection ratio with three different integrated optical devices based on ChG and Porous Germanium (PGe) materials with the same refractive indices as the ChG layers as a direct comparison for the large transparency windows in the Mid-IR. ChG and PGe ridge waveguides and ChG slot waveguides are explored in order to optimize sensor performance. The waveguide dimensions are therefore optimized to enhance the interaction between guided light and gas power factor while maintaining single-mode propagation in the Mid-IR. The LOD for each structure is calculated and compared to previously reported results.

2. Theory and proposed design

2.1 Principle of the gas detection scheme based on absorption bands in the Mid-IR.

The detection of gases depends on the absorption bands in the Mid-IR wavelength range. Each gas has one or more absorption peaks, known as the gas fingerprint. In our case for the three guiding integrated structures, the two gases studied are carbon dioxide (CO_2) and methane (CH_4). CO_2 has a high absorption peak at a wavelength of 4.3 µm while CH_4 has two absorption peaks at 3.3 and 7.7 µm [15].

Three integrated optical structures, presented in Figure 1, are studied: Ridge waveguides based on ChG materials (Figure 1.(a)), PGe material (Figure 1.(b)) and slots waveguides based on ChG (Figure 1.(c)). Waveguides (a) and (c) are fabricated on a Si substrate, while waveguide (b) is fabricated on a Ge substrate. The PGe layer porosities (and refractive index) of the ridge waveguide are respectively p_1 = 42% (n_1 =2.69) for the guiding layer and p_2 = 47% (n_2 =2.49) for the confinement layer.

Theses porosities were chosen so as to have refractive indices corresponding to those of ChG ridge waveguide based on the guiding layer material Se_4 and the confinement layer material Se_2, and calculated using Bruggeman model for effective index [10,41]. The structural dimensions wrail, g, h, and w correspond to the width of Se4 ChG regions,

width of the gap region, height of the waveguide, and the width of the waveguide, respectively.

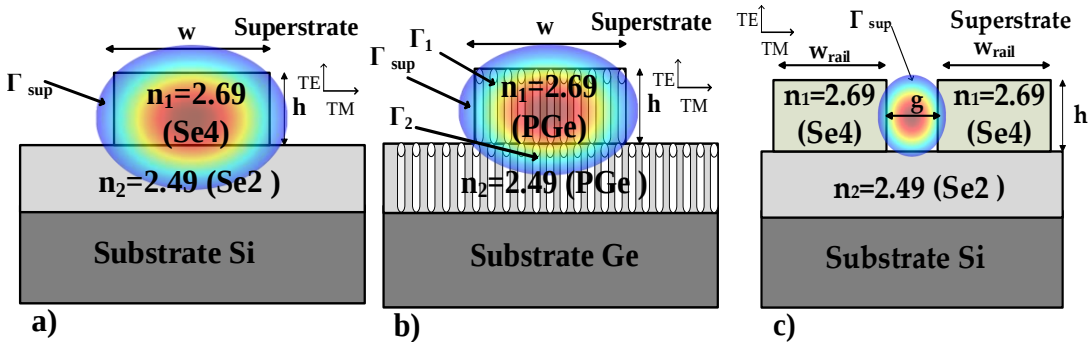

Figure 1. Types of waveguides investigated (a) ridge waveguide with ChG materials (b) ridge waveguide with PGe materials and (c) ChGs slot waveguide.

The detection mechanism consists of measuring the power in the optical output signal, which varies as a function of the absorption coefficient C (mol L^{-1}). Therefore, power attenuation increases with gas concentration levels and it is also directly dependent on light-gas interaction power factor η [42]. Γ_{sup} is defined as the ratio of the evanescent field power in the air superstrate to the total guided optical power. Γ_1 and Γ_2 represent, respectively, the interaction field power factor between the gas to detect and the fraction of total guided optical power in the guiding and confinement layers. Γ_1 and Γ_2 are defined schematically in Figure 1.(b) for the porous waveguide. In order to calculate the field distribution in the waveguide, the Full Vector Mode Solver FMM (film mode matching) of FIMMWAVE was used. The distribution of the field intensity in the superstrate, guiding and confinement layers relative to the total intensity are defined respectively as [40]:

$$\Gamma_{sup}(\lambda) = \frac{\iint_{sup} P_z dxdy}{\iint_{Total} P_z dxdy} \quad (1)$$

$$\Gamma_1(\lambda) = \frac{\iint_{guiding} P_z dxdy}{\iint_{Total} P_z dxdy} \quad (2)$$

$$\Gamma_2(\lambda) = \frac{\iint_{confinement} P_z dxdy}{\iint_{Total} P_z dxdy} \quad (3)$$

Where P_z is the Poynting vector along the propagation direction z, and Γ_{sup}, Γ_1 and Γ_2, obey the relation [40]:

$$\Gamma_{sup}(\lambda) + \Gamma_1(\lambda) + \Gamma_2(\lambda) = 1 \quad (4)$$

The power factor η(λ) can be expressed by:

$$\eta(\lambda) = \Gamma_{sup}(\lambda) + p_1\Gamma_1(\lambda) + p_2\Gamma_2(\lambda) \quad (5)$$

With p_1 and p_2 the porosities of respectively the guiding and confinement layers.

Parameters p_1 and p_2 only concern porous materials, therefore the evanescent field factor η(λ) is more important in PGe ridge waveguide compared to ChG ridge waveguide for which $\eta(\lambda) = \Gamma_{sup}$.

The wavelength corresponding to the absorption peak of the gas under study, the light travelling through the waveguide is attenuated. The examination of the transmission spectra of the propagating light covering the peak region of this gas allows us to identify it with great selectivity and sensitivity. The principle of wave absorption is one of the most widely used in optical sensors since it is possible associate the optical power P in a guiding structure under the concentration C of a substance. It is possible to associate the optical power P in a guiding structure with the concentration of a substance C using Beer-Lambert's law [10], this expression is wavelength-dependent λ and is written in the form:

$$P(\lambda) = P_0 \exp\left[-\eta(\lambda)\varepsilon(\lambda)C(\lambda)L(\lambda) - \alpha_{prop}L(\lambda)\right] \quad (6)$$

P0(W) is the optical power at the waveguide input, η (%) is the interaction power factor, α (cm^{-1}) corresponds to the propagation losses, L (cm) is the length of the waveguide interacting with the target molecules and ε is the molar absorption ($L.mol^{-1}$ cm^{-1}) which is associated with the absorption of the molecule A according to: A = C ε.

The sensitivity of the integrated optical sensor is defined as the ratio between the change in optical power and the change in concentration of the molecules to be detected. It is calculated by deriving equation (6) with respect to C [10]:

$$S = \left|\frac{dP}{dc}\right| = \varepsilon(\lambda)\,\eta(\lambda)\,L(\lambda)\,P_0 \exp\left[-\varepsilon(\lambda)\eta(\lambda)\,C(\lambda)\,L(\lambda) - \alpha_{prop}\,L(\lambda)\right] \quad (7)$$

For this expression, the condition $\alpha >> \eta\varepsilon C$ is accomplished for low concentration to be measured. Equation (7) reveals that the sensitivity is directly proportional to η and, therefore, can be improved by maximizing its value.

Sensitivity is also useful to determine the optimum waveguide length L_{opt}, which is found at the maximum of the S function and depends on the propagation loss. So, propagation loss α is also important in determining the optimal length of the guide L_{opt}, allowing the maximum sensitivity S to be obtained. The expression for calculating the optimal transducer interaction length L is given by [10]:

$$L_{opt} = \frac{1}{\varepsilon(\lambda)\eta(\lambda)C(\lambda)+\alpha} \quad (8)$$

If the previously imposed condition ($\alpha >> \eta\varepsilon C$) is fulfilled, L_{opt} depends essentially on α and can be approximated as, $L \approx 1/\alpha$. This equation reveals the impact of waveguide propagation losses on the sensor performance.

The minimum resolvable concentration C_{min} or LOD is given by the following expression [7]:

$$C_{min} = \frac{-\ln\left[1 - \frac{SNR \quad NEP \quad \sqrt{B}}{P_0 \exp(-\alpha_{prop}\,L_{opt}(\lambda))}\right]}{\varepsilon(\lambda)\,\eta(\lambda)\,L_{opt}(\lambda)} \quad (9)$$

The LOD (Cmin) is physically limited by the photodetector specifications, such as signal-to-noise ratio (SNR), noise equivalent power (NEP and bandwidth (B). The employed value of the photodetector are P_0(W) = 1 mW, SNR equal to 10, $NEP = 5\times10^{-12}\,W/Hz$, and $B = 5\,KHz$ [10]. $\varepsilon_{CO_2} = 2613\,L.mol^{-1}cm^{-1}$ [10] for CO_2 detection at 4.3 µm and $\varepsilon_{CH4} = 174\,L.mol^{-1}cm^{-1}$ [7] for CH_4 detection at 7.7 µm have been taken for the calculation; ε_{CO_2} and ε_{CH_4} are assumed to be constant over the range of concentration. The Signal to Noise Ratio (SNR) is fixed equal to 10 for this calculation. This SNR value is unfavorable considering the coupling loss at the waveguide input and output So, this SNR value was not dependent on the performance of the QCL.

2.2 Optimization of transducer dimensions

To achieve the best sensing performance, the power factor η has to be maximized through waveguide dimension (w, g, h, and w_{rail}) optimization. These waveguiding structures were designed using a commercial software (FIMMWAVE, Photon Design) to obtain the geometrical dimensions, width (w or w_{rail}) and height (h), allowing single mode propagation at wavelengths of 4.3 µm or 7.7 µm, while maximizing the power factor. All the simulations were performed when the waveguides are singlemode.

For the fabrication of these integrated devices, the chalcogenide thin films are subsequently deposited onto silicon substrates by RF magnetron sputtering. The multilayered structure was made of a -thick lower confinement layer and a low thick guiding layer while galvanostatic etching of germanium substrate is performed in a two electrode electrochemical cells with a Pt wire counter to fabricate porous germanium layers by using an electrolyte which is a volumic mixture of hydrofluoric acid ad anhydrous ethanol. Then, integrated waveguides of different widths were then fabricated using a classical i-line photolithographic process or by e-beam process according to device dimensions followed by a dry etching procedure at low pressure combining reactive ion etching (RIE) and inductively coupled plasma (ICP) etching.

Moreover, n inherent feature of porous germanium material is its open pore network. This can be used to modify the properties of optical devices in-situ, by filling the pores with other molecules. The pores are several nanometers in diameter to allow the infiltration of gas.

2.2.1 Optimization of the ridge waveguide dimensions at wavelengths of 4.3µm and 7.7µm

Silicon and germanium are transparent materials in the wave range [2-15µm]. Moreover, the refractive index n of these materials do not vary in the studied wavelength range [43,44].

For the simulation and for both studied wavelength, single mode ridge waveguides with refractive indices of n_1 = 2.69 and n_2 = 2.49, respectively for the guiding layer (ChG guiding layers in the case of ChG materials and PGe in the case of porous materials with a porosity p_1 = 0.42) and the lower confinement layer (in the case of ChG materials and

PGe in the case of porous materials with porosity a $p_2 = 0.47$) were considered. A refractive index $n_0 = n_{air} = 1$ is used for the superstrate as the presence of CH_4 or CO_2 at low concentration is not supposed to significantly affect the refractive index of air.

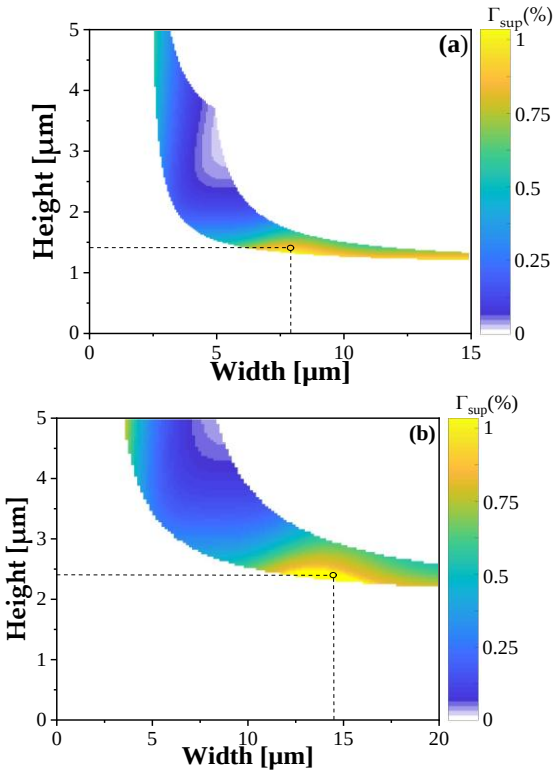

Figure 2. Evolution of the evanescent field factor of the evanescent wave Γ_{sup} as a function of geometrical dimensions (w,h) for TM polarization: (a) 4.3 µm (CO_2 detection) and (b) 7.7 µm (CH_4 detection) for ridge waveguide based on ChG or PGe materials with similar refractive indices.

The evolution of Γ_{sup} as a function of the geometrical parameters (w, h) of ChG waveguide, which allow single mode propagation is presented in Figure 2.(a) and 2.(b) at λ= 4.3 µm and at λ= 7.7 µm, wavelengths of interest for CO_2 and CH_4, respectively. As TM polarization represents an optimization in the sensor design by maximizing the power factor [10], only the results for this polarization are reported. Figure 2.(a) shows that the value of Γ_{sup} for the detection of CO_2 is maximum for waveguide widths w between 6.1 µm and 9.1 µm and for waveguide height h between 1.3 µm and 1.6 µm. A value of Γ_{sup} = 1% is obtained for the optimal dimensions of the waveguide of w = 7.9 µm and h = 1.4 µm.

For the detection of CH_4, Figure 2.(b) shows that the value of Γ_{sup} is maximum (1%) for waveguide widths w between 12 µm and 15 µm and for guide height h between 2.4 µm and 2.7 µm. The optimal dimensions of the waveguide are w = 14.4 µm and h = 2.4 µm. The TM polarization gives a larger evanescent field factor Γ_{sup}, hence its choice for this type of material.

Table 1 resumes the configuration parameters of a ridge waveguide for the TM polarization and for ChG or PGe materials. w_{opt} and h_{opt} correspond respectively to the width and the height of the ridge waveguide that induce a maximum power factor η. As the gas will infiltrate pores of the PGe waveguide, which exhibits p_1 and p_2 porosities for the confinement and guiding layers, respectively, the values of Γ_1 and Γ_2 have to be taken into account in the gas and were also calculated.

Polarization	Materials	w_{opt} (µm)	h_{opt} (µm)	N_{eff}	Γ_{sup} (%)	Γ_1 (%)	p_1	Γ_2 (%)	p_2	η (%)
TM4.3µm	ChG	7.9	1.4	2.50	1	-4.4	-0.42	-5.5	-0.47	14 5.3
TM 7.7µm	ChG PGe	14.4	2.4	2.49	1	-5.6	-0.42	-4.3	-0.47	14 4.7

Compared to ChG material, the PGe material displays a substantial increase in the η factor (45 %) calculated from equation (5). The porosities in the guiding and confinement layers induced an increase in the quantity of gas in the pores which allowed a better interaction of propagated light and gas.

2.2.2 Optimization of the slot waveguide dimensions at wavelengths of 4.3 µm and 7.7 µm

The power factor η is optimized depending on the geometry of a slot waveguide and in particular on the dimensions of the height h and width of rail w_{rail} of the slot waveguide and slot width g which are schematically displayed in Figure 1.(c). To achieve the best performance of the sensor, the evanescent field factor ($\eta = \Gamma_{sup}$) has to be maximized by determining the waveguide dimensions (w_{rail}, the gap g, and h) that allow a significant fraction of light to be confined in the slot region.

A ChG slot waveguide has with a guiding layer of refractive index $n_1 = 2.69$ and a confinement layer $n_2 = 2.49$ was considered in the simulations. Air is considered yet

again as superstrate (n_0 = 1) for both wavelengths 4.3 µm and 7.7 µm. In slot waveguides, only TE modes are studied.

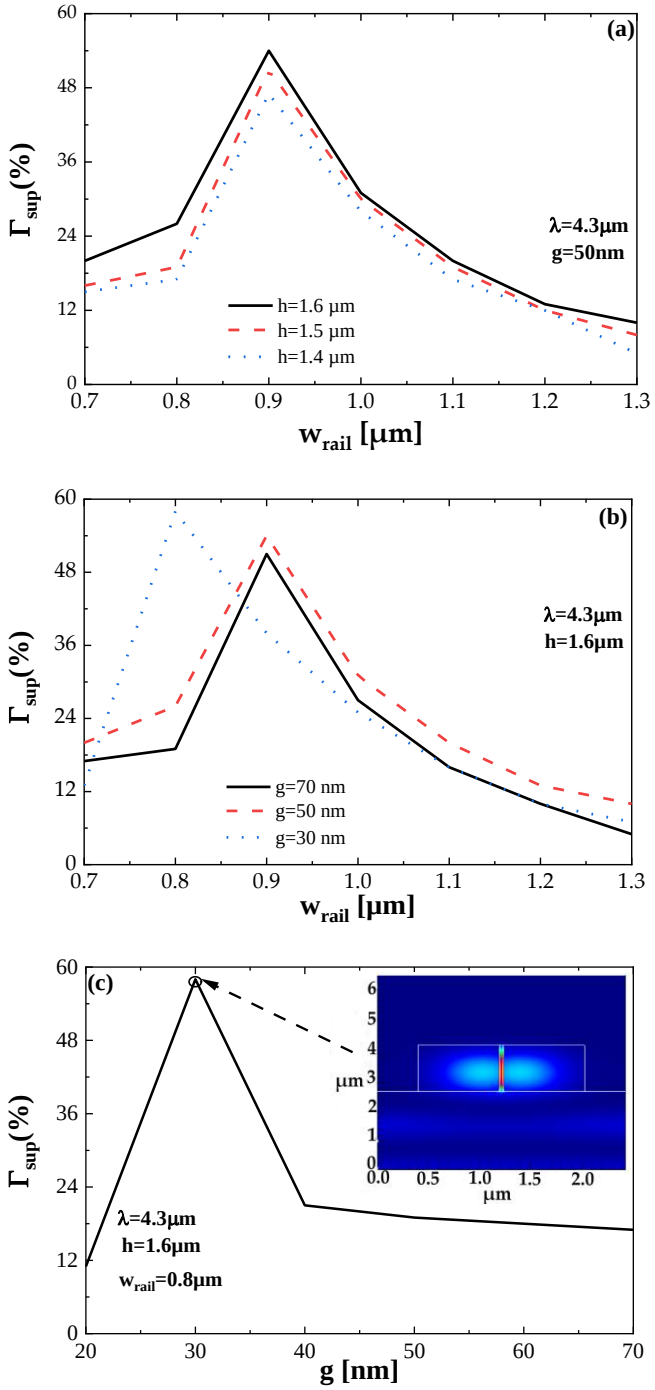

Figure 3. Optimization of Slot waveguides for CO_2 detection at 4.3 µm. The variation of Γ_{sup} as a function of the rail width w_{rail}, (a) for different values of h, (b) for different values of gap g and (c) Variation of Γ_{sup} as a function of g for the optimal values of w and h. The intensity profile of the proposed slot waveguide structures for g= 30nm is shown in the upper-right corner.

Figure 3.(c), in the upper-right corner, shows the intensity profile of the TE polarization propagated modes for the optimal dimensions. It is highly confined in the slot region g. The variation of Γ_{sup} with w for three different values of h and the width of the slot region g, and variation of Γ_{sup} with g for a fixed value of w and h are shown in Figure 3.(a), 3.(b), and 3.(c), respectively.

By examining these figures, it can be seen that the evanescent field factor reaches its maximum value for w_{rail} = 800 nm and for g=30 nm. For these values, a high value of the field is confined in the slot region. Figure 3(a) shows that the variation of h does not affect w_{opt}, which remains unchanged whatever h. W_{rail}, on the other hand, takes on greater values with the increase of g (Figure 3(b)). As the variation of h has no impact on w, the choice of h_{opt} = 1600 nm, for which Γ_{sup} is slightly better, is appropriate. When $w_{rail} < w_{opt}$. (Figure 3.(a) and 3.(c)) and $g < g_{opt}$ (Figure 3.(c)) a major fraction of the field penetrates into the confinement region and becomes evanescent, and hence, power factor decreases. For $w_{rail} > w_{opt}$ and $g > g_{opt}$, evanescent field factor decreases due to the stronger confinement of field inside the high index ChG. When $w_{rail} < w_{opt}$. (Figure 3.(a) and 3.(c)) and $g < g_{opt}$ (Figure 3.(c)) a major fraction of the field penetrates into the confinement region and becomes evanescent, and hence, power factor decreases. For $w_{rail} > w_{opt}$ and $g > g_{opt}$, evanescent field factor decreases due to the stronger confinement of field inside the high index ChG.

In order to have the best sensitivity, the optimal waveguide dimension chosen are: w_{rail} = 0.8 µm, h = 1.6µm, and g = 30 nm, for which η reach values as high as ~ 58 %.

For the wavelength of λ = 7.7 µm the same reasoning was followed. The optimal dimensions obtained are: w_{rail} = 0.9 µm, h = 1.9 µm and g = 90 nm. The corresponding η maximum factor is about 51%.

3. Results and discussion

3.1. Study of the performance of a ridge waveguide with ChG material for the two wavelengths 4.3 µm and 7.7 µm

The parameters taken into consideration, obtained previously are defined in Table 1 for CO_2 and CH_4 detection at 4.3 and 7.7 µm, respectively. In both cases, the maximum value of the evanescent field factor reached η = 1% for CO_2 detection and η = 1 % for CH_4 detection. Sensitivity S was calculated as a function of the concentration of target molecules in the range [400 – 800 ppm] and for propagation losses of 1, 3 and 6 dB/cm. Moreover, L_{opt} and LOD were calculated according to equation (8) and (9) respectively for each wavelength and optical loss and for C = 600 ppm corresponding to the studied target molecules concentration mid-range.

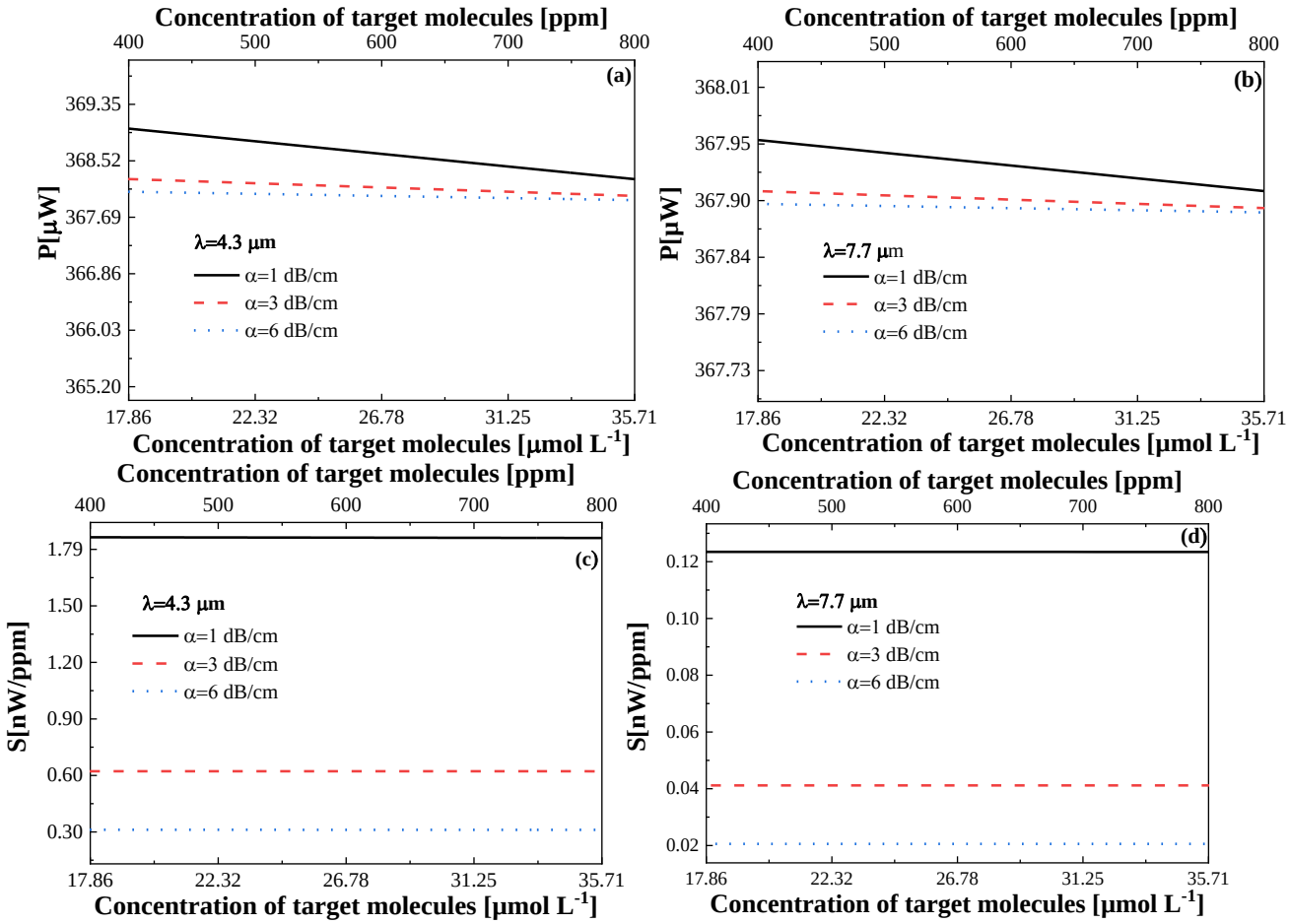

Figure 4. ChG ridge waveguide-based integrated sensor transmission and sensitivity as a function of the concentration C for several values of propagation loss α_{prop}. Evolution of the power P depending on concentration C of CO_2 at 4.3 µm (a) and of CH_4 at 7.7 µm (b). Evolution of the sensitivity S depending on concentration C of CO_2 at 4.3 µm (c) and of CH_4 at 7.7 µm (d).

The output power P and sensitivity S are plotted as a function of the concentration C in Figure 4 using equations (6) and (7) for different values of α_{prop}. Figure 4.(a) and 4.(c) show respectively the output power P and sensitivity S as a function of concentration C for CO_2 detection at 4.3 µm, whereas Figure 4.(b) and 4.(d) illustrate those of CH_4 detection at 7.7 µm. From these sensitivity curves, it is possible to appreciate the importance of the propagation losses of the ridge waveguide on the performance of the evanescent wave sensor. Indeed, low losses and the optimal interaction associated length allow a better interaction between the propagated light and the molecules in the superstrate and induce a higher sensitivity.

For CO_2 detection and propagation losses α_{prop} of 1 dB/cm and taking into account the optical interaction length L_{opt} of 4.33 cm, a sensitivity (S) is equal to 1.9 nW/ppm for a LOD of 1.87 ppm. For α_{prop} = 3 dB/cm, L_{opt} = 1.44 cm, S is equal to 0.62 nW/ppm for a LOD of 5.63 ppm. For α_{prop} = 6 dB/cm, a sensitivity of 0.31 nW/ppm is computed for a LOD of 11.27 ppm and L_{opt} = 0.72 cm.

For CH_4 detection and propagation losses α_{prop} of 1 dB/cm and L_{opt} = 4.34 cm, a sensitivity S equal to 0.12 nW/ppm is computed for a LOD of 28.22 ppm. For α_{prop} = 3 dB/cm and L_{opt} = 1.45 cm, S = 0.041 nW/ppm for a LOD of 84.65 ppm. Finally, for α_{prop} = 6 dB/cm and L_{opt} = 0.72 cm, S decreases to 0.02 nW/ppm for a LOD of 169.31 ppm.

The analysis of these results shows that the increase of propagation losses leads to a reduction in sensitivity and an increase of the LOD, which is undesirable. From Figure 4.(a) and 4.(b), a small variation in the output power is observed so the propagation losses do not have much influence on this parameter. Notice that the sensitivity is almost constant over the studied concentration range (Figure 4.(c) and 4.(d)). The LOD (in ppm) for CO_2 and CH_4 are 2 orders of magnitude lower than the threshold limit values (TLV) of 1000 ppm [14].

3.2. Study of the performance of a ridge waveguide made of PGe materials for the two wavelengths 4.3 µm and 7.7 µm

PGe is an interesting materiel because of its adjustable porosity, which can be modulated according to the fabrication parameters [45]. By changing the Ge porosity, PGe refractive index can be varied between the index of air and that of Ge material), which allows the design of optical waveguiding structures.

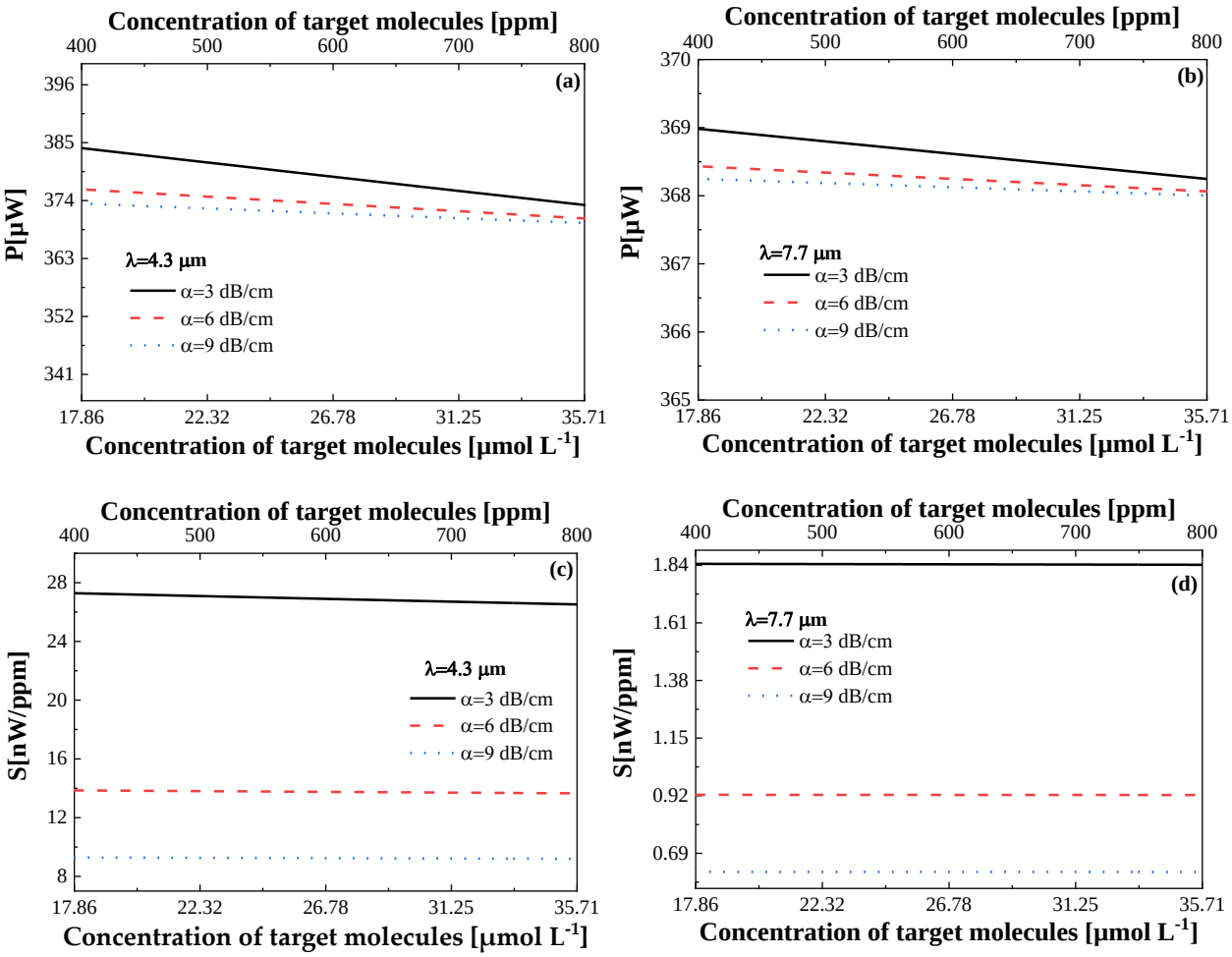

Figure 5. Power and sensitivity of the integrated sensor as a function of the concentration C for several values of propagation loss α_{prop} for PGe ridge waveguide. Evolution of the power P depending on concentration C of CO_2 at 4.3 µm (a) and of CH_4 at 7.7 µm (b). Evolution of the sensitivity S depending on concentration C of CO_2 at 4.3 µm (c) and of CH_4 at 7.7 µm (d).

For these simulations, the value of the power factor has been reached η = 45.3% for CO_2 and η = 44.7% for CH_4, the initial conditions from the previous section were also taken into account. Figure 5 shows the results obtained for output power P and sensitivity S, using equations (6) and (7) for different values of αprop. Figure 5.(a) and 5.(c) show respectively the output power P and sensitivity S as a function of concentration C for CO_2 detection at 4.3 µm, whereas Figure 5.(b) and 5.(d) illustrate those of CH_4 detection at 7.7 µm

Expected propagation losses α_{prop} are higher (the chosen values range from 3 to 9 dB/cm) than those used for the simulations of ChG waveguide and are mostly related to volume diffusion [38].

For CO_2 detection and propagation losses α_{prop} of 3 dB/cm with L_{opt}= 1.40 cm, the medium sensitivity (S) is 28 nW/ppm for a LOD of 0.12 ppm. For α_{prop} =6 dB/cm and L_{opt}= 0.71 cm, S is 14 nW/ppm for a detection limit of 0.25 ppm. Finally, for α_{prop} =9 dB/cm and L_{opt}= 0.47 cm, S = 9.4 nW/ppm for a detection limit of 0.37 ppm.

For CH_4 detection and propagation losses α_{prop} of 3 dB/cm with L_{opt} = 1.41 cm, a sensitivity S equal to 1.8 nW/ppm is computed for a LOD of 1.89 ppm. For α_{prop} =6 dB/cm and L_{opt} = 0.72cm, S = 0.92 nW/ppm for a LOD of 3.78 ppm. Finally, for α_{prop} = 9 dB/cm and L_{opt} = 0.48cm, S = 0.62 nW/ppm for a LOD of 5.66 ppm.

The analysis of these results shows better results compared to the previous ChG waveguide due to the increased interaction between the light and the molecules which infiltrate the pores and thus increasing the power factor η(λ) and consequently enhancing the sensitivity and the decrease of the LOD.

3.3. Study of the performance of a slot waveguide for the two wavelengths 4.3 µm and 7.7 µm

It has been shown in the optimization section and Figure 3 that for this type of ChG waveguide η is equal to 58% for a wavelength λ = 4.3 µm and 51% at λ = 7.7 µm. Figure 6.(a) and 6.(c) show respectively the output power P and sensitivity S as a function of concentration of CO_2 at 4.3 µm for 3 different values of propagation loss α_{prop}, whereas Figure 6.(b) and 6.(d) illustrate those of CH_4 at 7.7 µm.

For CO_2 detection and propagation losses α_{prop} of 1 dB/cm with L_{opt} = 3.88 cm, a sensitivity S equal to 100 nW/ppm is computed for a LOD of 0.034 ppm. For α_{prop} =3 dB/cm and L_{opt} = 1.39 cm, S is 35 nW/ppm for a detection limit of 0.1 ppm. Finally, for α_{prop} = 6 dB/cm and L_{opt}= 0.70 cm, we have S = 1.7 nW/ppm for a LOD of 0.19 ppm.

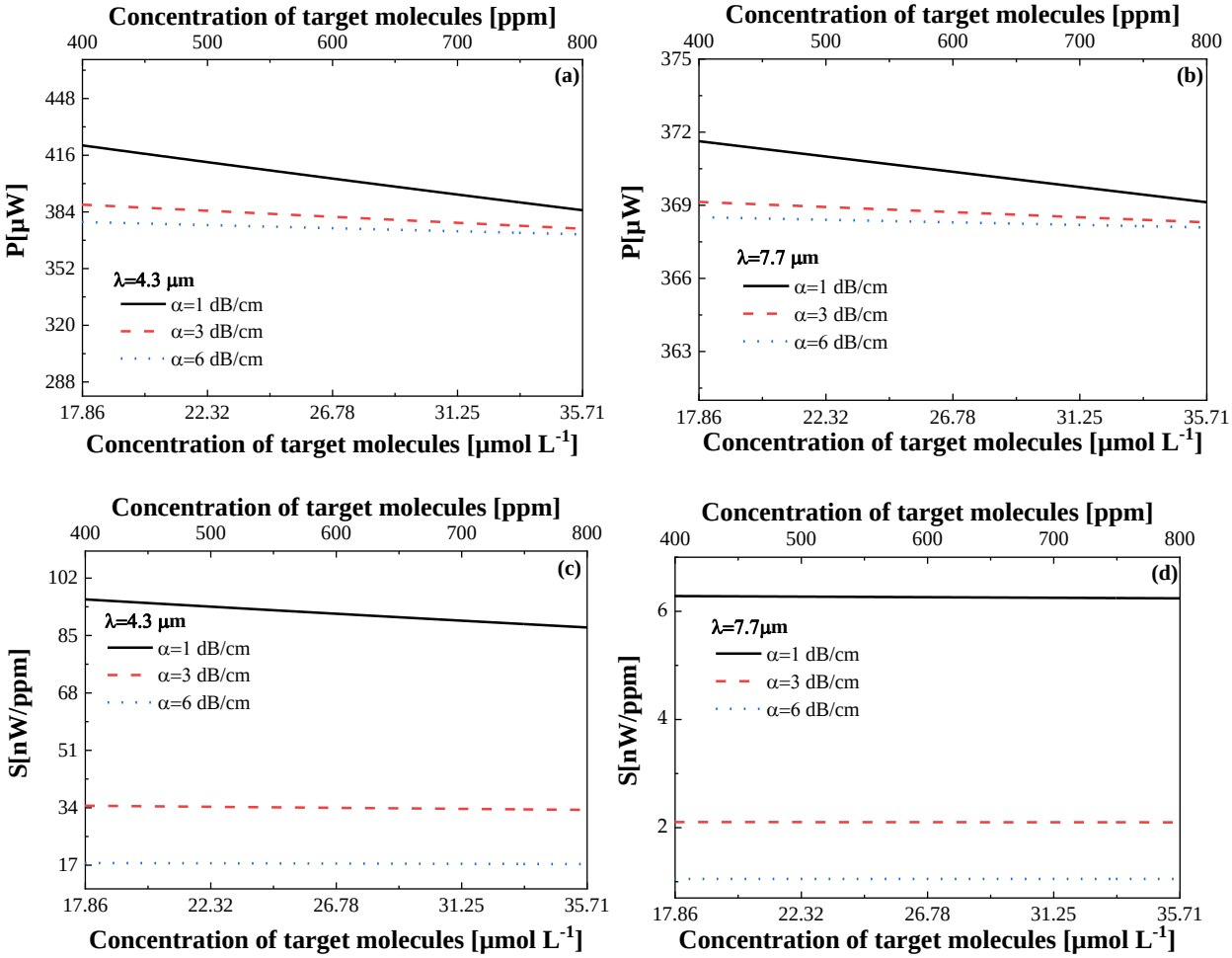

Figure 6. Power and sensitivity of the integrated sensor as a function of the concentration C for several values of propagation loss α_{prop} for slot waveguide. Evolution of the power P depending on concentration C of CO_2 at 4.3 µm (a) and of CH_4 at 7.7 µm (b). Evolution of the sensitivity S depending on concentration C of CO_2 at 4.3 µm (c) and of CH_4 at 7.7 µm (d).

For CH_4 detection and propagation losses α_{prop} of 1 dB/cm with L_{opt} =4.31 cm , a sensitivity S equal to 6.3 nW/ppm is computed for a LOD of 0.55 ppm. For α_{prop} = 3 dB/cm and L_{opt} = 1.44 cm, S = 2.1 nW/ppm for a LOD of 1.66 ppm. Finally, for α_{prop} = 6 dB/cm and L_{opt} = 0.72 cm, S = 1.1 nW/ppm for a LOD of 3.31 ppm.

In slot waveguide, the light is strongly confined in the slot region. The interaction between the target molecules and the light is then increased, improving sensitivity at the same time. The coupling losses reduce the transmitted power, which decreases the sensitivity.

Table 2 summarizes all the results for the 3 studied structures for α_{prop} = 3 dB/cm for CO_2 detection at 4.3 µm and for CH_4 detection at 7.7 µm. The different sensors studied are very sensitive, in particular the ChG-slot and PGe-ridge waveguides, which have very close results.

Table 2. Comparison of the sensitivity and the detection limit for the three waveguides studied with α_{prop} = 3 dB/cm at 4.3 µm and 7.7 µm.

waveguide	η(%)		Sensitivity (nW/ppm)		LOD (ppm)	
λ(µm)	**4.3**	**7.7**	**4.3**	**7.7**	**4.3**	**7.7**
ChG-ridge	1	1	0.62	0.041	5.63	84.65
PGe-ridge	4 5.3	4 4.7	28	1.8	0.12	1.89
ChG-slot	5 8	5 1	35	2.1	0.1	1.66

For ChG ridge waveguide configuration, the interaction of light with the gaseous detection medium takes place only in evanescent mode. Notice that the sensitivity of the porous material waveguide is almost comparable to the slot waveguide. The interaction of light with the gaseous environment is increased in these last two guiding structures.

Table 3. Limit of Detection (LOD) of the integrated chalcogenide glass sensor for CO_2 and CH_4 measurement in Mid-IR.

Reference	waveguide	Propagation loss	λ(µm) CO_2	LOD of CO_2	λ(µm) CH_4	LOD of CH_4	method	Year
[3]	ChG-slot	2 dB/cm	4.23	2 ppm	-	-	Theoretical	2014
[4]	ChG-ridge	3 dB/cm	2.5	10 ppm	-	-	Experimental	2017
[10]	ChG-ridge	1 dB/cm	4.3	0.26 ppm	7.7	1.9 ppm	Theoretical	2017
[8]	ChG-slot	3 dB/cm	-	-	3.31	1.7 ppm	Practical	2019
This work	PGe-ridge	3 dB/cm	4.3	0.12 ppm	7.7	1.89ppm	Theoretical	
This work	ChG-slot	3 dB/cm	4.3	0.10 ppm	7.7	1.66 ppm	Theoretical	

Table 3 reports our LOD results, which are compared with the state of the art in this field. The values for CH_4 detection are in the same order than the state of the art but lowest limit of detection for CO_2 values so far reported in the literature are obtained in this using work ridge PGe material and slot waveguide based on ChG material.

For the detection of CO_2, the results reported in Table 3, show that they are better than those reported in the literature (0.26 ppm for propagation losses of 3 dB/cm) for the reference [10]. For the porous germanium-based sensor, the detection limit is 0.12 ppm while for the waveguide slot the limit is 0.1 ppm for 3 dB/cm losses. For CH_4 detection, the results are comparable to those of the table items although the simulated structure was suffering from higher propagation losses.

5. Conclusion

The pertinence of developing optical sensors in the Mid-IR range is based on the presence of the vibrational absorption bands of many molecules in this wavelength

range, between 2 µm and 20 µm, thus enabling highly sensitive spectroscopic measurements for chemical analysis of target molecules for various applications such as health and environment. The development of new techniques for selective detection and high sensitivity in Mid-IR range is currently a focus of interest in industry and scientific research. In this context, devices designed in integrated optics have certain advantages over other types of sensors. In this paper, ridge and slot waveguides were optimized to obtain high power factor ratio to increase sensing detection rate of the proposed power field factor absorption gas sensor.

The materials chosen for the fabrication of these integrated platforms are chalcogenide glasses and porous germanium, which have a wide transparency in Mid-IR, a wide range of refractive index according to their composition and a relatively easy technological implementation.

The structure of the different types of waveguides, allows the molecules to interact with the evanescent wave in case of ChG and slot waveguide configurations. In porous waveguide configuration, the light interaction takes place not only with the evanescent wave but also with the light propagated in the guiding and confinement waveguide layers. In this last case, the porous configuration, the interaction between the light and the molecules is increased because molecules infiltrate the pores and thus increasing the interaction factor and consequently enhancing the sensitivity.

ChGs slot waveguides provide the highest sensitivity S = 35 nW/ppm for a detection limit of 0.1 ppm, for carbon dioxide at λ = 4.3 µm and S = 2.1 nW/ppm for a detection limit of 1.66 ppm for methane at λ = 7.7 µm when propagation losses α_{prop} = 3 dB/cm are assumed. The results from the PGe ridge waveguide are comparable with those obtained with ChG slot waveguide and are the most impressive. Indeed, this PGe material has a large specific surface area which resulted in good characteristics, particularly its sensitivity and detection limit.

These results indicate that the possible limit of detection represents, in some cases, one hundredth of the limit values recommended by international environmental standards [14], thus justifying the potential of these integrated sensor based on PGe or ChG materials as environmental monitoring tools. The detection could be improved by using lock-in detection by scanning over the absorption line or reference arm. The aim of the paper is to compare the performance of the three photonic structures using two types of materials for the integrated platform to improve to improve the detection of gas in the mid-infrared in term of optic power however the spectral resolution should be also improved [46].

Author Contributions: R. Z. carried out the simulations, wrote the paper, and prepared the original draft; N.L. and J.C. proposed the research directions. All authors contributed to the organization of the paper, writing, and proofreading. All authors read and agreed to the published version of the manuscript.

Funding: This work was supported by the French national research agency under MID-VOC ANR project (ANR-17-CE09-0028-01). Equipment funding of Institut Foton were partly provided by the CPER Sophie, and by Exceptional National Program (PNE) of Algerian ministry of higher education and scientific research.

Conflicts of Interest: The authors declare no conflicts of interest.

References

1. Majhi, S.M.; Mirzaei, A.; Kim, H.W.; Kim, S.S.; Kim, T.W. Recent advances in energy-saving chemiresistive gas sensors: A review. *Nano Energy* **2021**, *79*, 105369, doi:10.1016/j.nanoen.2020.105369.
2. Meng, Z.; Stolz, R.M.; Mendecki, L.; Mirica, K.A. Electrically-Transduced Chemical Sensors Based on Two-Dimensional Nanomaterials. *Chem. Rev.* **2019**, *119*, 478–598, doi:10.1021/acs.chemrev.8b00311.
3. Huang, Y.; Kalyoncu, S.K.; Zhao, Q.; Torun, R.; Boyraz, O. Silicon-on-sapphire waveguides design for mid-IR evanescent field absorption gas sensors. *Optics Communications* **2014**, *313*, 186–194, doi:10.1016/j.optcom.2013.10.022.
4. Hu, T.; Dong, B.; Luo, X.; Liow, T.-Y.; Song, J.; Lee, C.; Lo, G.-Q. Silicon photonic platforms for mid-infrared applications [Invited]. *Photon. Res., PRJ* **2017**, *5*, 417–430, doi:10.1364/PRJ.5.000417.
5. Han, Z.; Lin, P.; Singh, V.; Kimerling, L.; Hu, J.; Richardson, K.; Agarwal, A.; Tan, D.T.H. On-chip mid-infrared gas detection using chalcogenide glass waveguide. *Appl. Phys. Lett.* **2016**, *108*, 141106, doi:10.1063/1.4945667.
6. Tombez, L.; Zhang, E.J.; Orcutt, J.S.; Kamlapurkar, S.; Green, W.M.J. Methane absorption spectroscopy on a silicon photonic chip. *Optica, OPTICA* **2017**, *4*, 1322–1325, doi:10.1364/OPTICA.4.001322.
7. Gutierrez-Arroyo, A.; Baudet, E.; Bodiou, L.; Lemaitre, J.; Hardy, I.; Faijan, F.; Bureau, B.; Nazabal, V.; Charrier, J. Optical characterization at 7.7 µm of an integrated platform based on chalcogenide waveguides for sensing applications in the mid-infrared. *Opt. Express, OE* **2016**, *24*, 23109–23117, doi:10.1364/OE.24.023109.
8. Pi, M.; Zheng, C.; Bi, R.; Zhao, H.; Liang, L.; Zhang, Y.; Wang, Y.; Tittel, F.K. Design of a mid-infrared suspended chalcogenide/silica-on-silicon slot-waveguide spectroscopic gas sensor with enhanced light-gas interaction effect. *Sensors and Actuators B: Chemical* **2019**, *297*, 126732, doi:10.1016/j.snb.2019.126732.

9. Koompai, N.; Limsuwan, P.; Le Roux, X.; Vivien, L.; Marris-Morini, D.; Chaisakul, P. Analysis of Si3N4 waveguides for on-chip gas sensing by optical absorption within the mid-infrared region between 2.7 and 3.4 µm. *Results in Physics* **2020**, *16*, 102957, doi:10.1016/j.rinp.2020.102957.
10. Gutierrez-Arroyo, A.; Baudet, E.; Bodiou, L.; Nazabal, V.; Rinnert, E.; Michel, K.; Bureau, B.; Colas, F.; Charrier, J. Theoretical study of an evanescent optical integrated sensor for multipurpose detection of gases and liquids in the Mid-Infrared. *Sensors and Actuators B: Chemical* **2017**, *242*, 842–848, doi:10.1016/j.snb.2016.09.174.
11. Kumari, B.; Barh, A.; Varshney, R.K.; Pal, B.P. Silicon-on-nitride slot waveguide: a promising platform as mid-IR trace gas sensor. *Sensors and Actuators B: Chemical* **2016**, *236*, 759–764.
12. Frish, M.B.; Shankar, R.; Bulu, I.; Frank, I.; Laderer, M.C.; Wainner, R.T.; Allen, M.G.; Lončar, M. Progress toward mid-IR chip-scale integrated-optic TDLAS gas sensors. In Proceedings of the Quantum Sensing and Nanophotonic Devices X; International Society for Optics and Photonics, 2013; Vol. 8631, p. 86310E.
13. Khonina, S.N.; Kazanskiy, N.L.; Butt, M.A. Evanescent Field Ratio Enhancement of a Modified Ridge Waveguide Structure for Methane Gas Sensing Application. *IEEE Sensors Journal* **2020**, *20*, 8469–8476, doi:10.1109/JSEN.2020.2985840.
14. Dettenrieder, C.; Raichlin, Y.; Katzir, A.; Mizaikoff, B. Toward the Required Detection Limits for Volatile Organic Constituents in Marine Environments with Infrared Evanescent Field Chemical Sensors. *Sensors* **2019**, *19*, 3644, doi:10.3390/s19173644.
15. Gordon, I.E.; Rothman, L.S.; Hill, C.; Kochanov, R.V.; Tan, Y.; Bernath, P.F.; Birk, M.; Boudon, V.; Campargue, A.; Chance, K.V.; et al. The HITRAN2016 molecular spectroscopic database. *Journal of Quantitative Spectroscopy and Radiative Transfer* **2017**, *203*, 3–69, doi:10.1016/j.jqsrt.2017.06.038.
16. Mid-infrared integrated photonics on silicon: a perspective in: Nanophotonics Volume 7 Issue 2 (2017) Available online: https://www.degruyter.com/view/journals/nanoph/7/2/article-p393.xml (accessed on Apr 21, 2020).
17. Mashanovich, G.; Mitchell, C.; Soler Penadés, J.; Khokhar, A.; Littlejohns, C.; Cao, W.; Qu, Z.; Stanković, S.; Gardes, F.; Ben Masaud, T.; et al. Germanium mid-infrared photonic devices. *Journal of Lightwave Technology* **2017**, *35*, 624–630, doi:10.1109/JLT.2016.2632301.
18. Marris-Morini, D.; Vakarin, V.; Ramirez, J.M.; Liu, Q.; Ballabio, A.; Frigerio, J.; Montesinos, M.; Alonso-Ramos, C.; Roux, X.L.; Serna, S.; et al. Germanium-based integrated photonics from near- to mid-infrared applications. *Nanophotonics* **2018**, *7*, 1781–1793, doi:10.1515/nanoph-2018-0113.
19. Ivanov, S.V.; Chernov, M.Yu.; Solov'ev, V.A.; Brunkov, P.N.; Firsov, D.D.; Komkov, O.S. Metamorphic InAs(Sb)/InGaAs/InAlAs nanoheterostructures grown on GaAs for efficient mid-IR emitters. *Progress in Crystal Growth and Characterization of Materials* **2019**, *65*, 20–35, doi:10.1016/j.pcrysgrow.2018.12.001.
20. Singh, V.; Lin, P.T.; Patel, N.; Lin, H.; Li, L.; Zou, Y.; Deng, F.; Ni, C.; Hu, J.; Giammarco, J. Mid-infrared materials and devices on a Si platform for optical sensing. *Science and technology of advanced materials* **2014**, *15*, 014603.
21. Chang, Y.-C.; Paeder, V.; Hvozdara, L.; Hartmann, J.-M.; Herzig, H.P. Low-loss germanium strip waveguides on silicon for the mid-infrared. *Optics letters* **2012**, *37*, 2883–2885.
22. Sieger, M.; Mizaikoff, B. Toward On-Chip Mid-Infrared Sensors. *Anal. Chem.* **2016**, *88*, 5562–5573, doi:10.1021/acs.analchem.5b04143.
23. Wang, Q.; Rogers, E.T.F.; Gholipour, B.; Wang, C.-M.; Yuan, G.; Teng, J.; Zheludev, N.I. Optically reconfigurable metasurfaces and photonic devices based on phase change materials. *Nature Photonics* **2016**, *10*, 60–65, doi:10.1038/nphoton.2015.247.
24. Vighnesh, K.R.; Ramya, B.; Nimitha, S.; Wagh, A.; Sayyed, M.I.; Sakar, E.; Yakout, H.A.; Dahshan, A.; Kamath, S.D. Structural, optical, thermal, mechanical, morphological & radiation shielding parameters of Pr3+ doped ZAlFB glass systems. *Optical Materials* **2020**, *99*, 109512, doi:10.1016/j.optmat.2019.109512.
25. Starecki, F.; Charpentier, F.; Doualan, J.-L.; Quetel, L.; Michel, K.; Chahal, R.; Troles, J.; Bureau, B.; Braud, A.; Camy, P. Mid-IR optical sensor for CO2 detection based on fluorescence absorbance of Dy3+: Ga5Ge20Sb10S65 fibers. *Sensors and Actuators B: Chemical* **2015**, *207*, 518–525.
26. Petersen, C.R.; Møller, U.; Kubat, I.; Zhou, B.; Dupont, S.; Ramsay, J.; Benson, T.; Sujecki, S.; Abdel-Moneim, N.; Tang, Z. Mid-infrared supercontinuum covering the 1.4–13.3 µm molecular fingerprint region using ultra-high NA chalcogenide step-index fibre. *Nature Photonics* **2014**, *8*, 830.
27. Lin, H.; Li, L.; Zou, Y.; Danto, S.; Musgraves, J.D.; Richardson, K.; Kozacik, S.; Murakowski, M.; Prather, D.; Lin, P.T. Demonstration of high-Q mid-infrared chalcogenide glass-on-silicon resonators. *Optics letters* **2013**, *38*, 1470–1472.
28. S, L.K.A.; S, L.K.A.; Mere, V.; Mere, V.; Selvaraja, S.K.; Raghunathan, V. Polarization-independent angle-tolerant mid-infrared spectral resonance using amorphous germanium high contrast gratings for notch

filtering application. *OSA Continuum, OSAC* **2020**, *3*, 1194–1203, doi:10.1364/OSAC.390644.

29. Demetriou, G.; Bérubé, J.-P.; Vallée, R.; Messaddeq, Y.; Petersen, C.R.; Jain, D.; Bang, O.; Craig, C.; Hewak, D.W.; Kar, A.K. Refractive index and dispersion control of ultrafast laser inscribed waveguides in gallium lanthanum sulphide for near and mid-infrared applications. *Opt. Express, OE* **2016**, *24*, 6350–6358, doi:10.1364/OE.24.006350.
30. Kanou, M.; Kameoka, T.; Suehara, K.; Hashimoto, A. Mid-infrared spectroscopic analysis of saccharides in aqueous solutions with sodium chloride. *Bioscience, Biotechnology, and Biochemistry* **2017**, *81*, 735–742, doi:10.1080/09168451.2016.1277943.
31. Mayer, A.S.; Phillips, C.R.; Langrock, C.; Klenner, A.; Johnson, A.R.; Luke, K.; Okawachi, Y.; Lipson, M.; Gaeta, A.L.; Fejer, M.M.; et al. Offset-Free Gigahertz Midinfrared Frequency Comb Based on Optical Parametric Amplification in a Periodically Poled Lithium Niobate Waveguide. *Phys. Rev. Applied* **2016**, *6*, 054009, doi:10.1103/PhysRevApplied.6.054009.
32. Mayerhöfer, T.G.; Pahlow, S.; Popp, J. Structures for surface-enhanced nonplasmonic or hybrid spectroscopy. *Nanophotonics* **2020**, *9*, 741–760, doi:10.1515/nanoph-2020-0037.
33. Takayama, O. MID-INFRARED NANOPHOTONICS FOR BIOCHEMICAL SENSING: A REVIEW. *Romanian Reports in Physics* **2020**, *72*, 408.
34. Hillbrand, J.; Andrews, A.M.; Detz, H.; Strasser, G.; Schwarz, B. Coherent injection locking of quantum cascade laser frequency combs. *Nature Photonics* **2019**, *13*, 101–104, doi:10.1038/s41566-018-0320-3.
35. Su, P.; Han, Z.; Kita, D.; Becla, P.; Lin, H.; Deckoff-Jones, S.; Richardson, K.; Kimerling, L.C.; Hu, J.; Agarwal, A. Monolithic on-chip mid-IR methane gas sensor with waveguide-integrated detector. *Appl. Phys. Lett.* **2019**, *114*, 051103, doi:10.1063/1.5053599.
36. Ari, J.; Starecki, F.; Boussard-Plédel, C.; Doualan, J.-L.; Quétel, L.; Michel, K.; Braud, A.; Camy, P.; Chahal, R.; Bureau, B.; et al. Rare-earth-doped chalcogenide glasses for mid-IR gas sensor applications. In Proceedings of the Optical Components and Materials XIV; International Society for Optics and Photonics, 2017; Vol. 10100, p. 101000Q.
37. Shaw, L.B.; Cole, B.; Thielen, P.A.; Sanghera, J.S.; Aggarwal, I.D. Mid-wave IR and long-wave IR laser potential of rare-earth doped chalcogenide glass fiber. *IEEE Journal of Quantum Electronics* **2001**, *37*, 1127–1137, doi:10.1109/3.945317.
38. Liu, Q.; Tu, X.; Kim, K.W.; Kee, J.S.; Shin, Y.; Han, K.; Yoon, Y.-J.; Lo, G.-Q.; Park, M.K. Highly sensitive Mach–Zehnder interferometer biosensor based on silicon nitride slot waveguide. *Sensors and Actuators B: Chemical* **2013**, *188*, 681–688.
39. Liu, Y.; Salemink, H.W.M. All-optical on-chip sensor for high refractive index sensing. *Appl. Phys. Lett.* **2015**, *106*, 031116, doi:10.1063/1.4906576.
40. Azuelos, P.; Girault, P.; Lorrain, N.; Dumeige, Y.; Bodiou, L.; Poffo, L.; Guendouz, M.; Thual, M.; Charrier, J. Optimization of porous silicon waveguide design for micro-ring resonator sensing applications. *J. Opt.* **2018**, *20*, 085301, doi:10.1088/2040-8986/aad01b.
41. Optical loss study of porous silicon and oxidized porous silicon planar waveguides: Journal of Applied Physics: Vol 101, No 8 Available online: https://aip.scitation.org/doi/abs/10.1063/1.2718886 (accessed on Jun 24, 2020).
42. Butt, M.A.; Khonina, S.N.; Kazanskiy, N.L. Silicon on silicon dioxide slot waveguide evanescent field gas absorption sensor. *Journal of Modern Optics* **2018**, *65*, 174–178, doi:10.1080/09500340.2017.1382596.
43. Němec, P.; Olivier, M.; Baudet, E.; Kalendová, A.; Benda, P.; Nazabal, V. Optical properties of (GeSe2)100−x(Sb2Se3)x glasses in near- and middle-infrared spectral regions. *Materials Research Bulletin* **2014**, *51*, 176–179, doi:10.1016/j.materresbull.2013.11.050.
44. Refractive index of silicon and germanium and its wavelength and temperature derivatives: Journal of Physical and Chemical Reference Data: Vol 9, No 3 Available online: https://aip.scitation.org/doi/abs/10.1063/1.555624 (accessed on Oct 12, 2020).
45. Bioud, Y.A.; Boucherif, A.; Belarouci, A.; Paradis, E.; Fafard, S.; Aimez, V.; Drouin, D.; Arès, R. Fast growth synthesis of mesoporous germanium films by high frequency bipolar electrochemical etching. *Electrochimica Acta* **2017**, *232*, 422–430, doi:10.1016/j.electacta.2017.02.115.
46. Alaa Fathy, Yasser M. Sabry, Sébastien Nazeer, Tarik Bourouina and Diaa A. Khalil . 0n-chip parallel Fourier transform spectrometer for broadband selective infrared spectral sensing, Microsystems & Nanoengineering volume 6, Article number: 10 (2020)